

**Buoyancy-driven instabilities around miscible  $A+B\rightarrow C$  reaction fronts: A general classification**

P. M. J. Trevelyan, C. Almarcha, and A. De Wit

*Nonlinear Physical Chemistry Unit, Center for Nonlinear Phenomena and Complex Systems, Faculté des Sciences, Université libre de Bruxelles (ULB), CP 231, 1050 Brussels, Belgium*

(Received 29 July 2014; published 2 February 2015)

Upon contact between miscible solutions of reactants  $A$  and  $B$  along a horizontal interface in the gravity field, various buoyancy-driven instabilities can develop when an  $A + B \rightarrow C$  reaction takes place and the density varies with the concentrations of the various chemicals. To classify the possible convective instability scenarios, we analyze the spatial dependence of the large time asymptotic density profiles as a function of the key parameters of the problem, which are the ratios of diffusion coefficients and of solutal expansion coefficients of species  $A$ ,  $B$ , and  $C$ . We find that 62 different density profiles can develop in the reactive problem, whereas only 6 of them can be obtained in the nonreactive one.

DOI: [10.1103/PhysRevE.91.023001](https://doi.org/10.1103/PhysRevE.91.023001)

PACS number(s): 47.20.Bp, 82.40.-g, 47.70.Fw, 47.55.P-

**I. INTRODUCTION**

Chemical reactions can induce buoyancy-driven convection when concentration gradients yield unfavorable density gradients in the gravity field [1,2]. In the case of miscible solutions and a simple  $A + B \rightarrow C$  reaction, related reaction-diffusion-convection (RDC) dynamics have recently been studied both experimentally [3–12] and theoretically [8–18]. In vertically oriented systems, when a solution of  $A$  overlies a solution of  $B$  in the gravity field, the reaction has been shown to modify the symmetry of the classical hydrodynamic instabilities [8,12]. The fact that a third species,  $C$ , is produced as time passes by can also profoundly modify the density profiles *in situ* and lead to observing different successive instabilities in the course of time [12]. Moreover, the fact that all three species  $A$ ,  $B$ , and  $C$  usually have different diffusion coefficients can trigger nonmonotonic density profiles, which provides the possibility of localized convective zones [8–12].

To appreciate all of the possibilities offered by such a simple  $A + B \rightarrow C$  reaction in modifying the convective dynamics with regard to the nonreactive case, let us first recall the situation expected in nonreactive systems. In the gravity field, various buoyancy-driven instabilities can develop around a horizontal miscible interface between two nonreactive solutions. When a denser fluid is placed above a less dense one along a horizontal interface (Fig. 1), a Rayleigh-Taylor (RT) instability occurs, deforming the interface into finger-shaped convective currents [19,20]. In the reverse case, i.e., when a less dense fluid is placed above a miscible denser one, instabilities can occur due to differential diffusion effects [20–24]. In the case of a vertical interface (i.e., parallel to the gravity field) between solutions of  $A$  and  $B$  of different density, convection always sets in, with the denser solution sinking below the less dense one in a gravity current that mixes the two fluids and spreads continuously in time.

The modifications of these convective dynamics when an  $A + B \rightarrow C$  reaction actively modifies the density have been studied in different limits. If the initial contact line is vertical, i.e., when the two solutions are side by side, Rongy *et al.* [13,14] found that six different types of density profiles were possible when all of the species diffuse at the

same rate. For equal initial concentrations, they found that one could analytically predict the number of convective rolls (0, 1, or 2) and the preferred reaction front direction using the known results for the one-dimensional reaction front. In the case of a horizontal interface (Fig. 1), various different scenarios have already been found. As an example, if a less dense solution of an acid is put on top of a denser solution of a base, differential diffusion and production of a salt of intermediate density yields an asymmetric density profile with a localized minimum located above the initial contact line and around which convection rolls develop. The resulting buoyancy-driven chemical pattern shows fingers rising *above* the interface [8–12]. In other systems, such as in the presence of a color indicator for instance, convection can also be observed *below* the initial contact line because of the buildup of a local maximum in this zone [3,10].

These observations, sustained by theoretical modeling of the specific problem at hand, show that, obviously, the reactive systems allow for much more instability scenarios than the nonreactive one simply because it deals with a three-species ( $A, B, C$ ) problem rather than only two as in the nonreactive one. There is, however, a lack of general understanding of the number of possible instability scenarios and for which values of parameters they are expected.

In this context, we provide here a general theoretical classification of the various types of buoyancy-driven instabilities that can be induced by a simple isothermal  $A + B \rightarrow C$  chemical reaction at the miscible horizontal interface between solutions of reactants  $A$  and  $B$ . To do so, the density profiles are reconstructed on the basis of asymptotic reaction-diffusion profiles, computed as large time solutions of the related reaction-diffusion problem. We show that 62 different density profiles can be obtained in the parameter space spanned by the ratio of diffusion coefficients and solutal expansion of the chemical species. The density profiles derived here provide the base states to be used for future linear stability analysis of the related RDC problem.

In Sec. II, the theoretical model is presented, while the various types of base-state density profiles are derived in Sec. III along with the conditions for the onset of a double-diffusive instability.

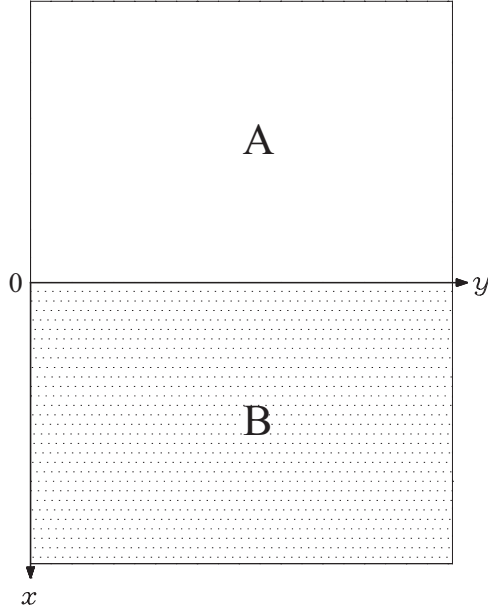


FIG. 1. Sketch of a two-dimensional cut in the system.  $x$  points vertically along the gravity field, while  $y$  is the horizontal direction.

## II. MODEL

We consider a vertically orientated system (Fig. 1), in which a solution containing a reactant  $A$ , of concentration  $A_0$ , is put above a solution containing a reactant  $B$ , of concentration  $B_0$ , along a horizontal contact line at time  $t = 0$ . By diffusion, the reactants meet and react via the scheme



to generate a product  $C$ . The equations describing the RDC dynamics of the concentrations  $A, B$ , and  $C$  of the corresponding species are

$$\frac{\partial A}{\partial t} + \underline{u} \cdot \underline{\nabla} A = D_A \nabla^2 A - qAB, \quad (2a)$$

$$\frac{\partial B}{\partial t} + \underline{u} \cdot \underline{\nabla} B = D_B \nabla^2 B - qAB, \quad (2b)$$

$$\frac{\partial C}{\partial t} + \underline{u} \cdot \underline{\nabla} C = D_C \nabla^2 C + qAB, \quad (2c)$$

where  $q$  is the kinetic constant and  $D_{A,B,C}$  are the molecular diffusion coefficients of species  $A, B$ , and  $C$ , respectively. To complement the model, a flow equation for the velocity field  $\underline{u}$  must be given in two dimensions (2D) or 3D typically Navier-Stokes equations, in general, or Darcy's law for flows in porous media, along with boundary conditions depending on the geometry. In buoyancy-driven instabilities in reactive systems, the interplay between reactions and hydrodynamics is achieved through the fact that the density  $\rho$  acting in the buoyancy term  $\rho \underline{g}$  is a function of the concentrations [8, 12, 13].

Here, the solutions are considered sufficiently dilute so that nonideal effects can be ignored, i.e., the diffusion coefficients are constant and the density  $\rho$  varies linearly with the concentrations as

$$\rho = \rho_0[1 + \gamma_A A + \gamma_B B + \gamma_C C], \quad (3)$$

where  $\rho_0$  is the density of the pure solvent and the molar expansion coefficients  $\gamma_i$  are defined as

$$\gamma_i = \frac{1}{\rho_0} \frac{\partial \rho}{\partial C_i},$$

where  $C_i$  is the concentration of the relevant chemical species. For simplicity, we assume the  $\gamma_i$ 's are positive so that the presence of each solute increases the density.

The spatial domain is considered infinite so that the initial conditions can be expressed as

$$A = A_0, \quad B = 0, \quad C = 0 \quad \text{for } x < 0,$$

$$A = 0, \quad B = B_0, \quad C = 0 \quad \text{for } x > 0,$$

where  $x < 0$  is the upper region above the contact line and  $x > 0$  is the lower region, as shown in Fig. 1.

For convenience, we nondimensionalize the equations using  $\hat{t} = t/T$ ,  $\hat{x} = x/\mathcal{L}$ ,  $\hat{u} = \underline{u}/\mathcal{U}$ ,  $[a, b, c] = [A, B, C]/A_0$ , where hats denote a dimensionless quantity and  $g = |\underline{g}|$ . The time and length scalings are given by

$$T = \frac{D_A}{\mathcal{U}^2} \quad \text{and} \quad \mathcal{L} = \frac{D_A}{\mathcal{U}},$$

respectively, where the typical velocity scaling  $\mathcal{U}$  is chosen according to how the flow is modeled. Additionally, the dimensionless density is given by  $\hat{\rho} = (\rho - \rho_0)/(\rho_0 \gamma_A A_0)$ . Substituting these nondimensional quantities into Eqs. (2) and (3) and dropping hats for convenience leads to the dimensionless model

$$\rho = a + R_b b + R_c c, \quad (4a)$$

$$a_t + \underline{u} \cdot \underline{\nabla} a = \nabla^2 a - \mathcal{D} ab, \quad (4b)$$

$$b_t + \underline{u} \cdot \underline{\nabla} b = \delta_b \nabla^2 b - \mathcal{D} ab, \quad (4c)$$

$$c_t + \underline{u} \cdot \underline{\nabla} c = \delta_c \nabla^2 c + \mathcal{D} ab, \quad (4d)$$

along with dimensionless flow equations involving  $\underline{u}$ . The initial conditions now become

$$a = 1, \quad b = 0, \quad c = 0 \quad \text{for } x < 0, \quad (4e)$$

$$a = 0, \quad b = \varphi, \quad c = 0 \quad \text{for } x > 0, \quad (4f)$$

where  $\varphi = B_0/A_0$  is the ratio between the initial concentrations of  $A$  and  $B$ . In addition to  $\varphi$ , other parameters of interest for the classification of instability scenarios are two diffusion coefficient ratios  $\delta_{b,c}$  and the Damköhler number  $\mathcal{D}$  given by

$$\delta_b = \frac{D_B}{D_A}, \quad \delta_c = \frac{D_C}{D_A}, \quad \mathcal{D} = q A_0 T,$$

respectively. The Damköhler number  $\mathcal{D}$  is the ratio between the characteristic hydrodynamic time scale  $T$  and the chemical time scale  $1/(qA_0)$ .

The dimensionless density  $\rho(a, b, c)$  involves two additional parameters, i.e., the expansion coefficient ratios

$$R_b = \frac{\gamma_B}{\gamma_A}, \quad R_c = \frac{\gamma_C}{\gamma_A}$$

expressing the relative weight of equimolar solutions of  $B$  or  $C$  with regard to an equimolar solution of  $A$ . Initially the upper pure solution of  $A$  has a density  $\bar{\rho} = 1$ , while the lower layer of  $B$  features a density  $\bar{\rho} = \varphi R_b$ . If  $\varphi R_b < 1$ , the initial stratification implies that there is a denser solution of  $A$  on

top of a less dense solution of  $B$  which is right away unstable with respect to a Rayleigh-Taylor (RT) instability. We seek here to understand how, in general, an  $A + B \rightarrow C$  reaction can destabilize situations of less dense  $A$  on top of denser  $B$  ( $\varphi R_b > 1$ ) as a function of the six dimensionless parameters  $R_b, R_c, \delta_b, \delta_c, \varphi$ , and  $\mathcal{D}$ .

We will therefore derive the various density profiles that can build up in time upon diffusion and reaction of the two reactants  $A$  and  $B$  to yield  $C$ , in the case  $\varphi R_b > 1$ . The equivalent profiles in the initially RT unstable case  $\varphi R_b < 1$  can trivially be obtained by turning the obtained profiles upside down.

### III. BASE STATE OF THE SYSTEM

Let us now analyze the concentration base states of the system and reconstruct the related density profile to help identify any sources of instability in the system. If the system is in a stable configuration, no disturbances grow, there is no fluid flow, and we can assume that the concentration fields are only functions of  $x$  and  $t$ . The resulting one-dimensional reaction-diffusion (RD) base-state solutions can be computed by solving the RD equations (4b)–(4d) with  $\underline{u} = 0$  along with the initial conditions (4e) and (4f). We let  $\bar{a}(x, t), \bar{b}(x, t)$ , and  $\bar{c}(x, t)$  denote the base-state concentrations, to allow the dimensionless base-state density profiles to be reconstructed as

$$\bar{\rho}(x, t) = \bar{a} + R_b \bar{b} + R_c \bar{c}. \quad (5)$$

Such base states can be obtained numerically to perform linear stability analyses, for instance. However, they can also give information on potential instabilities that typically develop dynamically in time in zones where locally  $\partial \bar{\rho} / \partial x < 0$ . This indeed signals the presence locally of a buoyantly unstable stratification of a denser zone on top of a less dense one, which is typically prone to give rise to convection. To identify the values of parameters for which such zones with unfavorable density gradients can develop (and their localization with regard to the initial contact line), we examine each of the limits  $t \rightarrow 0, \mathcal{D} \rightarrow 0, t \rightarrow \infty$ , and  $\mathcal{D} \rightarrow \infty$  for which the base-state solutions approach self-similar profiles, with

$$\eta = \frac{x}{2\sqrt{t}}$$

being the similarity variable. The first limits  $t \rightarrow 0$  or  $\mathcal{D} \rightarrow 0$  address the situations where the RD processes do not dominate and the hydrodynamic instabilities take place first. This is indeed typically the case when the Damköhler number tends to zero (no reaction effect) or at early times when RD processes have not yet had time to impact the density profiles. We recover then the hydrodynamic instabilities described in Sec. III A and for which the known base states given in Fig. 2 provide good agreement with experimental results (see [20,24], for instance).

On the contrary, if the Damköhler number tends to infinity (the reaction time is then much shorter than the hydrodynamic one), the reaction has time to operate to construct the RD density profiles before the hydrodynamic instability sets in. Then, either the system is initially RT unstable (denser on top of less dense) and the extrema triggered by the RD nonmonotonic profile can modify the symmetry of the pattern,

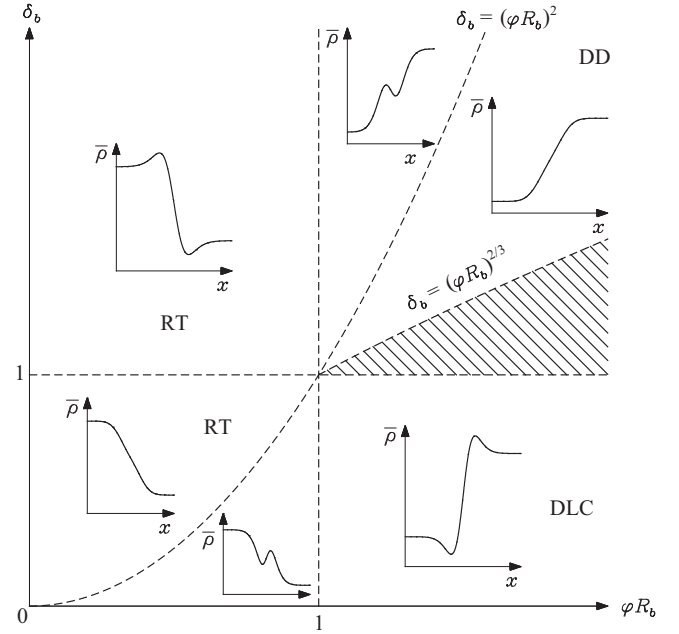


FIG. 2. Density profiles in the nonreactive case. If  $\varphi R_b \leq 1$ , we have a denser over less dense case, yielding a RT instability. If  $\varphi R_b \geq 1$ , the less dense over denser stratification can become unstable towards either a DD or a DLC mechanism.

provided the density difference is not too large [12], or the system is initially stable (less dense on top of denser) and can certainly be affected by local unfavorable zones where  $\partial \bar{\rho} / \partial \eta < 0$ . The asymptotic profiles give the locations where this happens. A good agreement between what is observed experimentally and what the asymptotic RD profile predicts has already been obtained in the specific case of acid and base systems and of color indicators [8–12].

Our objective here is to generalize this strategy to any possible cases. To do so, let us then seek to gain insight into the dependence of  $\bar{\rho}$  on  $R_{b,c}$  and  $\delta_{b,c}$  and analyze the shape of asymptotic density profiles in both nonreactive and reactive cases.

#### A. Nonreactive case

If the reaction is slow (i.e., in the small Damköhler number limit) or in the small time limit, the reaction does not really affect the dynamics and the reactive term can be neglected from the leading order equations. In the limit of  $\mathcal{D} \rightarrow 0$ , the nonreactive case is recovered. The base-state profiles then have classical analytical pure diffusive solutions [25] given by

$$\bar{a} = \frac{1}{2} \operatorname{erfc}(\eta), \quad \bar{b} = \frac{\varphi}{2} \operatorname{erfc}\left(-\frac{\eta}{\sqrt{\delta_b}}\right), \quad \bar{c} = 0. \quad (6)$$

Combining Eqs. (5) and (6), one recovers the fact that, in this case, the gradient of the base-state density  $\bar{\rho}$  is symmetric about  $\eta = 0$  and the resulting hydrodynamic patterns are typically developing convective flows that extend as much upwards as downwards in the gravity field [20–22,24]. The condition for a RT instability (denser over less dense; Fig. 2) is  $\varphi R_b \leq 1$ , while an initially stratificationally stable situation is obtained in the reverse case. In the RT zone, differential diffusion effects

can induce in time nonmonotonic density profiles (Fig. 2), provided  $\delta_b > 1$  or  $\delta_b < (\varphi R_b)^2$  [24].

In the  $\varphi R_b > 1$  case, if the lower region initially contains the slower diffusing species, i.e.,  $\delta_b < 1$ , then a diffusive-layer convection (DLC) instability develops with convective motions appearing symmetrically above and below the initial contact line in the zones of unfavorable density gradients of the nonmonotonic profile, i.e., in the locations where  $\partial\bar{\rho}/\partial x < 0$  (Fig. 2). If the lower region initially contains the faster diffusing species, i.e.,  $\delta_b > 1$ , then nonmonotonic density profiles exist provided  $\delta_b > (\varphi R_b)^2$ . A double-diffusive (DD) instability can develop around the initial contact line, even when  $\partial\bar{\rho}/\partial x > 0$  (Fig. 2). If the two species  $A$  and  $B$  have constant concentration gradients  $\partial A/\partial x$  and  $\partial B/\partial x$ , respectively, the condition for such a DD instability is [21,26]

$$-\frac{R_B (\partial B/\partial x)}{R_A (\partial A/\partial x)} < \frac{D_B}{D_A}, \quad (7)$$

where  $D_A$  and  $D_B$  are their respective diffusion coefficients and  $R_A$  and  $R_B$  are their respective solutal expansion coefficients.

One can use this inequality to predict the conditions for an instability in our nonreactive system by approximating the concentration gradients by their maximum values. Using  $\partial\bar{a}/\partial x = -(4\pi t)^{-1/2}$  and  $\partial\bar{b}/\partial x = \varphi(4\pi\delta_b t)^{-1/2}$ , which are the concentration gradients at  $x = 0$ , one finds that the only region of the parameter space which remains stable for all time is

$$1 \leq \delta_b^{3/2} \leq \varphi R_b. \quad (8)$$

Although in many circumstances one wants to induce convection to increase mixing, there are also situations when, in fact, one wants to avoid convection, and so Eq. (8) provides the conditions required to avoid any buoyancy-induced convection for a nonreactive system. Figure 2 shows that the nonreactive case is thus limited to six different density profiles (three with the denser zone on top and three with the denser part on the bottom).

### B. Reactive case

In diffusion limited problems, the reaction  $A + B \rightarrow C$  induces a reaction zone. Within the reaction zone, the reaction front is generally defined as the position where the reaction rate is largest. If the reaction is fast, i.e., in the large Damköhler number limit or in the large time limit, the base-state solutions outside the reaction zone have been obtained analytically. Gálfi and Rácz [27] first showed that when the diffusion coefficients are equal, the position  $x_f$  of the reaction front scales with  $\sqrt{t}$  while the width of the reaction front scales with  $t^{1/6}$ . Thus, on the diffusive length scale, which scales with  $\sqrt{t}$ , the width of the reaction front tends to zero. This allowed them to construct a solution outside the reaction zone in which no reaction takes place and set the two reactant concentrations to zero at the position of the reaction front. Koza [28] extended their study to unequal diffusion coefficients to obtain the large time asymptotic reactant solutions, while Sinder and Pelleg [29] obtained the solution for the product. Explicitly, the center of the reaction front is at

$$x_f = 2\alpha\sqrt{t}, \quad (9)$$

where  $\alpha$  is a constant depending on  $\delta_b$  and  $\varphi$ . If  $\alpha = 0$ , the front remains localized at the point of initial contact between the solutions of  $A$  and  $B$ . If  $\alpha > 0$  ( $< 0$ ), then the front moves downwards (upwards). The large time asymptotic base-state solutions are [28,29]

$$\bar{a}^U = 1 - \frac{\text{erfc}(-\eta)}{\text{erfc}(-\alpha)}, \quad \bar{c}^U = \frac{\text{erfc}(-\eta/\sqrt{\delta_c})}{\text{erfc}(-\alpha/\sqrt{\delta_c})}, \quad (10a)$$

$$\bar{b}^L = 1 - \frac{\text{erfc}(\eta/\sqrt{\delta_b})}{\text{erfc}(\alpha/\sqrt{\delta_b})}, \quad \bar{c}^L = \frac{\text{erfc}(\eta/\sqrt{\delta_c})}{\text{erfc}(\alpha/\sqrt{\delta_c})}, \quad (10b)$$

with  $\bar{b}^U = \bar{a}^L = 0$  and where the superscripts  $U$  and  $L$  denote the upper solutions (above the reaction front,  $\eta < \alpha$ ) and lower solutions (below the reaction front,  $\eta > \alpha$ ), respectively. The constant  $\beta$  is given by

$$\beta = e^{\alpha^2(\delta_c^{-1}-1)} \frac{\text{erfc}(\alpha/\sqrt{\delta_c})\text{erfc}(-\alpha/\sqrt{\delta_c})}{2\sqrt{\delta_c}\text{erfc}(-\alpha)}, \quad (10c)$$

and  $\alpha$  is the solution of the equation

$$e^{\alpha^2(\delta_b^{-1}-1)}\text{erfc}(\alpha/\sqrt{\delta_b}) = \varphi\sqrt{\delta_b}\text{erfc}(-\alpha). \quad (10d)$$

We note that the direction of the reaction front is determined by the sign of  $(1 - \varphi^2\delta_b)$ ; see [28]. When  $\varphi\sqrt{\delta_b} = 1$ , i.e., explicitly when  $A_0^2 D_A = B_0^2 D_B$ , then, in the large time asymptotic limit, the position of the reaction front is stationary ( $\alpha = 0$ ). When  $(1 - \varphi^2\delta_b)$  is positive, the front moves downwards as  $\alpha > 0$ , and the reverse occurs when it is negative.

If the system is stable for a long period of time before an instability occurs, then we can approximate the base-state solutions in the upper ( $U$ ) and lower ( $L$ ) parts by their large time asymptotic solutions given by Eq. (10). These large time asymptotic base-state solutions can be used to obtain the density as  $\bar{\rho}^U = \bar{a}^U + R_c \bar{c}^U$  and  $\bar{\rho}^L = R_b \bar{b}^L + R_c \bar{c}^L$ , i.e., explicitly,

$$\bar{\rho}^U = \left[ 1 - \frac{\text{erfc}(-\eta)}{\text{erfc}(-\alpha)} \right] + R_c \beta \frac{\text{erfc}(-\eta/\sqrt{\delta_c})}{\text{erfc}(-\alpha/\sqrt{\delta_c})},$$

$$\bar{\rho}^L = \varphi R_b \left[ 1 - \frac{\text{erfc}(\eta/\sqrt{\delta_b})}{\text{erfc}(\alpha/\sqrt{\delta_b})} \right] + R_c \beta \frac{\text{erfc}(\eta/\sqrt{\delta_c})}{\text{erfc}(\alpha/\sqrt{\delta_c})}.$$

As it is much easier to determine the properties of the density by examining its derivative  $d\rho/d\eta$  [13,30], we next examine it in detail:

$$\frac{d\bar{\rho}^U}{d\eta} = -\frac{2e^{-\eta^2}}{\sqrt{\pi}\text{erfc}(-\alpha)} + \frac{2\beta R_c e^{-\eta^2/\delta_c}}{\sqrt{\pi}\delta_c \text{erfc}(-\alpha/\sqrt{\delta_c})},$$

$$\frac{d\bar{\rho}^L}{d\eta} = \frac{2\varphi R_b e^{-\eta^2/\delta_b}}{\sqrt{\pi}\delta_b \text{erfc}(\alpha/\sqrt{\delta_b})} - \frac{2\beta R_c e^{-\eta^2/\delta_c}}{\sqrt{\pi}\delta_c \text{erfc}(\alpha/\sqrt{\delta_c})}.$$

Let us now see whether this profile admits extrema either above or below the reaction front.

#### 1. Above the reaction front

Above the reaction front, the density has a local extremum when  $d\bar{\rho}^U/d\eta = 0$  in  $\eta < \alpha$ . This extremum may occur at  $\eta^2 = E_U$  where

$$E_U = \frac{\delta_c}{1 - \delta_c} \ln(R_c/U_1),$$

with

$$U_1 = U_2 e^{\alpha^2(1-\delta_c^{-1})} \quad \text{and} \quad U_2 = \frac{2\delta_c}{\text{erfc}(\alpha/\sqrt{\delta_c})}.$$

If  $\alpha > 0$  and  $\eta < \alpha$ , then there are two points which satisfy  $d\bar{\rho}^U/d\eta = 0$  when  $0 < E_U < \alpha^2$ , one point when  $E_U > \alpha^2$ , and no points when  $E_U < 0$ . The dividing curves  $E_U = 0$  and  $E_U = \alpha^2$  are, respectively, given by

$$R_c = U_1, \quad R_c = U_2. \quad (11)$$

These two curves cross at the point  $\delta_c = 1$  with  $R_c = 2/\text{erfc}(\alpha)$ . However, if  $\alpha = 0$ , then the condition for a local extremum is  $(2\delta_c - R_c)(\delta_c - 1) > 0$  and, hence, one only needs to consider the lines  $\delta_c = 1$  and  $R_c = 2\delta_c$ .

If  $\alpha < 0$  and  $\eta < \alpha$ , then there is one point which satisfies  $d\bar{\rho}^U/d\eta = 0$  when  $E_U > \alpha^2$  and no points when  $E_U < \alpha^2$ . Now  $E_U = \alpha^2$  is the only dividing line.

In Fig. 3, the large time asymptotic density profiles *above the reaction front* are classified by their types of extrema. Six types of base-state density profiles exist when the reaction front moves downwards [ $\alpha > 0$ ; Fig. 3(a)]. These profiles can be monotonic or feature one or two extremas. Only four different base-state density profiles exist when the reaction front is stationary or moves upwards [ $\alpha \leq 0$ ; Fig. 3(b)]. Such profiles are either monotonic or include a single extremum.

These density profiles can be physically explained. First, if  $\delta_c < 1$ , it means that species *C* diffuses slower than species *A*, leading to a minimum in the density profile between the reaction front and the upper pure solution of *A* where the fast escape downwards of *A* has not been compensated by diffusion of *C* upwards. However, when the relative contribution of *C* to density is increased (increasing  $R_c$ ), this local minimum becomes less and less dominant. Conversely, if  $\delta_c > 1$ , then species *C* diffuses faster than *A*, which can lead to a local maximum in the density profile between the reaction front and the upper liquid when the density of species *C* is not too large. At large  $R_c$ , the much denser *C* produced in the reaction front leads to an increase of the density at  $\eta = 0$ . Note that when  $\alpha > 0$  [Fig. 3(a)], i.e., when the front moves downwards because  $A_0^2 D_A > B_0^2 D_B$ , the differential flux of *A* and *B* towards the reactive zone explains why two extrema can be obtained in the intermediate values of  $R_c$ , leading to six different possible profiles. If  $\alpha < 0$  [Fig. 3(b)], then  $A_0^2 D_A < B_0^2 D_B$  and the larger flux of *B* towards the reaction zone leads to the upward motion of the front but also hinders the possibility of two extrema, allowing only four profiles to be obtained. These density profiles allow one to see for which range of parameters there is a zone where  $d\bar{\rho}/d\eta < 0$  features a local stratification of denser on top of less dense, which is prone to develop an instability.

A stratifically stable density profile is only possible above the reaction front when  $\delta_c > 1$  and

$$\begin{aligned} R_c &> U_1 \quad \text{for} \quad \alpha > 0, \\ R_c &> U_2 \quad \text{for} \quad \alpha < 0. \end{aligned}$$

However, just as in the nonreactive case, even a stratifically stable density profile can induce an instability due to differential diffusive effects. The corresponding neutral stability condition

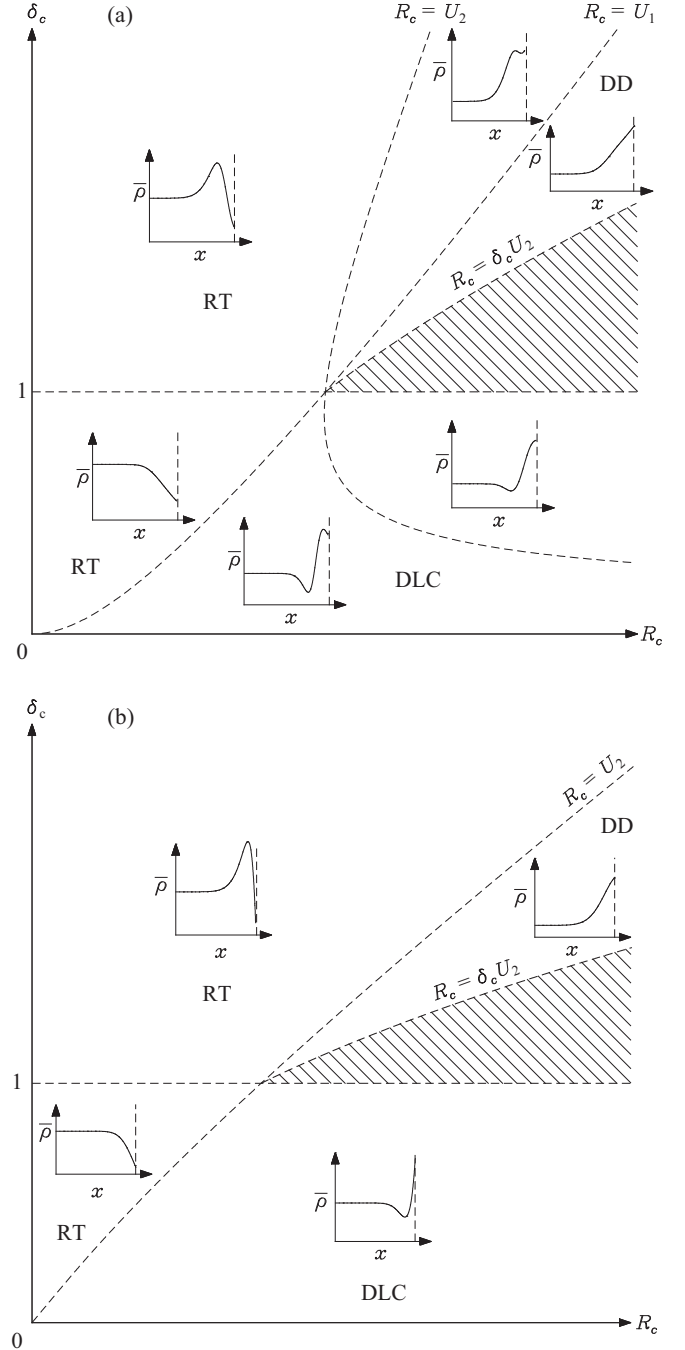


FIG. 3. Classification of the large time asymptotic base-state density profiles above the reaction front, i.e., in  $\eta < \alpha$ . The direction of the reaction front is (a) downwards, i.e.,  $\alpha > 0$  and (b) stationary ( $\alpha = 0$ ) or upwards ( $\alpha < 0$ ). The shaded area corresponds to the stable region.

can be obtained analytically in the large time asymptotic limit. As the instability will be focused in the region where the concentration gradients are largest, one can approximate the various large time asymptotic concentration profiles by their profiles at the reaction front, near  $x = 2\alpha\sqrt{t}$ . Thus, above the reaction front, we can approximate the gradients of the

concentration by

$$\frac{d\bar{a}^U}{d\eta} = -\Lambda, \quad \frac{d\bar{b}^U}{d\eta} = 0, \quad \frac{d\bar{c}^U}{d\eta} = \frac{\Lambda}{U_2},$$

in the large time limit, where  $\Lambda^{-1} = e^{\alpha^2} \sqrt{\pi} \operatorname{erfc}(-\alpha)$ . When a solution of  $A$  overlies a solution of  $B$ , the condition for a DD instability to occur when linear concentration profiles are present is given by Eq. (7). Using the large time asymptotic linear gradients at the reaction front in the region above the reaction front, the condition becomes  $-(R_c \partial \bar{c} / \partial x) / (\partial \bar{a} / \partial x) < \delta_c$ , which means that a DD instability can occur above the reaction front when

$$R_c < \delta_c U_2 \tag{12}$$

so that the product is not too dense. This condition was used to determine the stable region in Fig. 3. Such regions are anticipated to be stable as they have a monotonic increasing density profile and a DD instability is not possible.

### 2. Below the reaction front

Below the reaction front, the density has a local extremum when  $d\bar{\rho}^L / d\eta = 0$  in  $\eta > \alpha$ , with the extremum occurring at  $\eta^2 = E_L$  where

$$E_L = \frac{\delta_c \delta_b}{\delta_c - \delta_b} \ln(R_b L_1 / R_c),$$

with

$$L_1 = L_2 e^{\alpha^2 (\delta_b^{-1} - \delta_c^{-1})} \quad \text{and} \quad L_2 = \frac{2\delta_c}{\delta_b \operatorname{erfc}(-\alpha / \sqrt{\delta_c})}.$$

If  $\alpha < 0$  and  $\eta > \alpha$ , then there are two points which satisfy  $d\bar{\rho}^L / d\eta = 0$  when  $0 < E_L < \alpha^2$ , one point when  $E_L > \alpha^2$ , and no points when  $E_L < 0$ . The dividing lines  $E_L = 0$  and  $E_L = \alpha^2$  are, respectively, given by

$$\frac{R_c}{R_b} = L_1, \quad \frac{R_c}{R_b} = L_2. \tag{13}$$

These two curves cross at the point  $\delta_c = \delta_b$  with  $R_c / R_b = 2 / \operatorname{erfc}(-\alpha / \sqrt{\delta_c})$ .

However, if  $\alpha = 0$ , then the condition for a local extremum is  $(2\delta_c R_b - \delta_b R_c)(\delta_c - \delta_b) > 0$  and, hence, one only needs to consider the lines  $\delta_c = \delta_b$  and  $R_c = 2\delta_c R_b / \delta_b$ .

If  $\alpha > 0$  and  $\eta > \alpha$ , then there is one point which satisfies  $d\bar{\rho}^L / d\eta = 0$  when  $E_L > \alpha^2$  and no points when  $E_L < \alpha^2$ . Now  $E_L = \alpha^2$  is the only dividing line.

In Fig. 4, the large time asymptotic density profiles *below the reaction front* are classified by their types of extrema. As an echo of the situation described in Fig. 3 above the front, we see that now only four different types of base-state density profiles exist below the front when the reaction front is stationary or moving downwards [ $\alpha \geq 0$ ; Fig. 4(a)], while six different profiles can develop when the reaction front moves upwards [ $\alpha < 0$ ; Fig. 4(b)].

Again, some of these density profiles can be physically explained. If  $\delta_b / \delta_c < 1$ , then species  $C$  diffuses faster than species  $B$ , leading to a larger density at  $\eta = 0$  when  $R_b / R_c$  is small. When the contribution of  $B$  to the density becomes progressively more important than that of  $C$  (i.e., when  $R_b / R_c$  increases), the value of  $\bar{\rho}$  at  $\eta = 0$  decreases. A maximum can

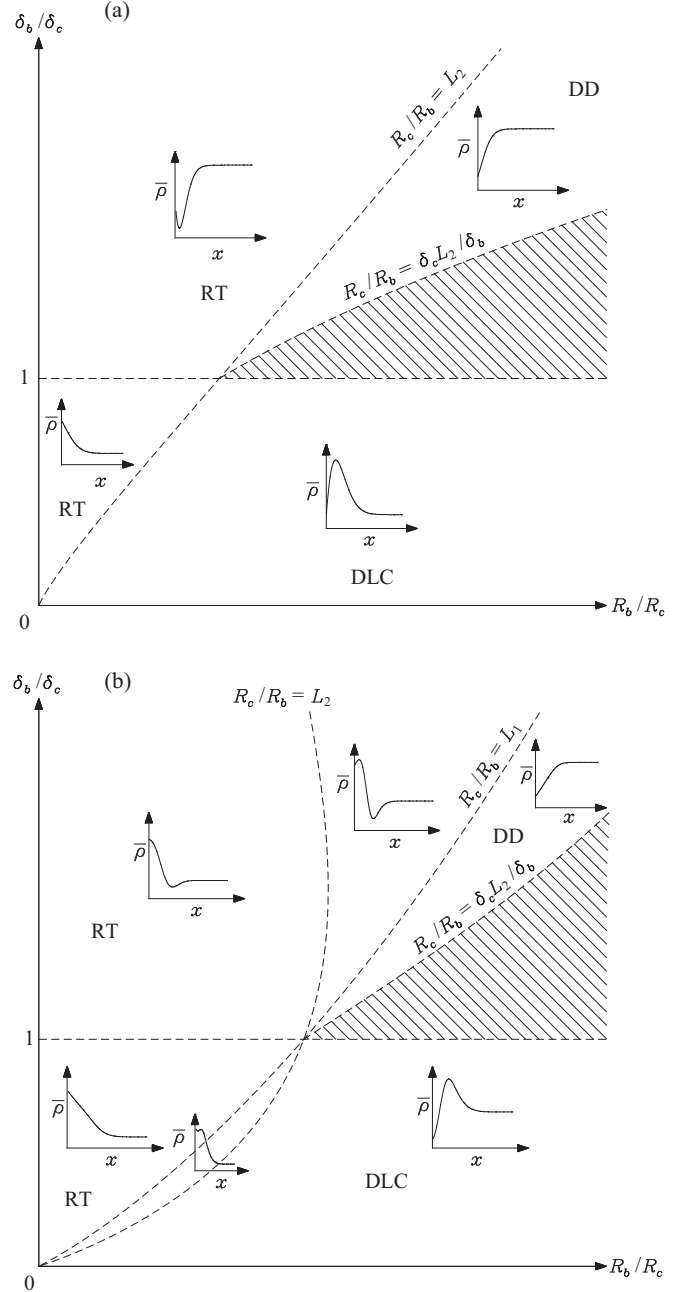


FIG. 4. Classification of the large time asymptotic base-state density profiles below the reaction front, i.e., in  $\eta > \alpha$ . The direction of the reaction front is (a) stationary ( $\alpha = 0$ ) or downwards ( $\alpha > 0$ ) and (b) upwards, i.e.,  $\alpha < 0$ . The shaded area corresponds to the stable region.

then develop below the front because  $B$  diffuses too slowly from the bulk to fill in the decrease caused by its replacement by a less dense  $C$  in the reaction front. In the intermediate regime of  $R_b / R_c$ , two extrema can be obtained if  $\alpha < 0$ . When  $\delta_b / \delta_c > 1$ , then species  $C$  diffuses faster than  $B$ , which can lead to a local minimum in the density profile between the reaction front and the lower liquid when the density of species  $C$  is sufficiently large ( $R_b / R_c$  small). On the contrary, a monotonically increasing density is obtained if  $R_b / R_c$  is large enough.

A stratifically stable density profile is only possible below the reaction front when  $\delta_b/\delta_c > 1$  and

$$\frac{R_c}{R_b} < L_1 \text{ for } \alpha < 0,$$

$$\frac{R_c}{R_b} < L_2 \text{ for } \alpha > 0.$$

Again, a stratifically stable density profile can induce an instability due to differential diffusive effects. Now, below the reaction front, we approximate the gradients of the concentration by

$$\frac{d\bar{a}^L}{d\eta} = 0, \quad \frac{d\bar{b}^U}{d\eta} = \frac{\Lambda}{\delta_b}, \quad \frac{d\bar{c}^U}{d\eta} = -\frac{\Lambda}{\delta_b L_2}.$$

Using these large time asymptotic linear gradients at the reaction front in the region below the reaction front, the condition becomes  $-(R_b \partial \bar{b} / \partial x) / (R_c \partial \bar{c} / \partial x) < (\delta_b / \delta_c)$ , which means that a DD instability can occur below the reaction front when

$$\frac{R_c}{R_b} > \frac{\delta_c}{\delta_b} L_2, \quad (14)$$

so that the product is sufficiently dense. This condition was used to determine the stable regions in Fig. 4. Such regions are anticipated to be stable as they have a monotonic increasing density profile and a double-diffusive instability is not possible.

### 3. Global base-state density profiles

In the previous two sections, we have separately classified the different types of base-state density profiles possible, respectively, above and below the reaction front by the type of extrema featured.

In the case of a stationary reaction front ( $\alpha = 0$ ), there are four different types of density profiles both below [Fig. 4(a)] and above [Fig. 3(b)] the reaction front. Combining them leads thus, when starting from a solution of  $A$  on top of a denser solution of  $B$ , to a total of 16 different types of density profiles over the whole domain, as illustrated in Fig. 5. Intuitively,

this can be understood as the 16 different combinations possible when playing with two different diffusion coefficients (horizontal axis of Fig. 5) and two different soluble expansion coefficient ratios (vertical axis of Fig. 5) submitted to the condition  $\delta_b = 1/\varphi^2$  fixed by the condition  $\alpha = 0$ . Physically, some cases can easily be understood: if the product  $C$  is the less dense species and diffuses the slowest, then a nonmonotonic profile with a minimum in the reaction zone is formed (top, left corner of Fig. 5). Shifts of the extremum position above or below the reaction front are obtained if  $A$  diffuses the slowest or the fastest (second and third panels, respectively, in column 1 of Fig. 5). More than one extremum is obtained if the slow diffusion  $C$  is the densest one (last panel in column 1 of Fig. 5). The other cases can be explained by similar arguments. Reversing the situation of Fig. 5 by turning it upside down, i.e., starting from a denser solution of  $A$  on top of a less dense solution of  $B$ , gives an additional 16 profiles with the two monotonic ones being the same. Hence, 30 different density profiles can be obtained in the case of a stationary front ( $\alpha = 0$ ).

When the reaction front is moving, then there are six different types of density profiles behind the reaction front and four different types of density profiles ahead of it. As an example, the six profiles of Fig. 3(a) above the reaction front must be combined with the four profiles of Fig. 4(a) below the front. This leads to a total of 32 different types of density profiles, which consists of the 16 ( $4 \times 4$ ) profiles included in Fig. 5 (constructed with the half profiles of Figs. 3 and 4 with only one extremum) plus the additional 16 profiles constructed from the cases when two extrema occur behind the reaction front. We note that there are not 36 ( $6 \times 6$ ) profiles, as there cannot be two extrema ahead of the reaction front.

Again, this classification has not discriminated between the cases of denser on top of less dense and the reverse less dense on top of denser. Thus, for a moving reaction front, there are a total of 62 different types of density profiles, which comes from  $2 + 2 \times 30$ , as 30 of the profiles can occur in the denser on top of less dense situation and the reverse case, but the two cases with monotonic profiles can only occur once.

As a final comment, we note that in order for the entire density profile to be monotonically increasing, we require that  $\delta_b > \delta_c > 1$  and

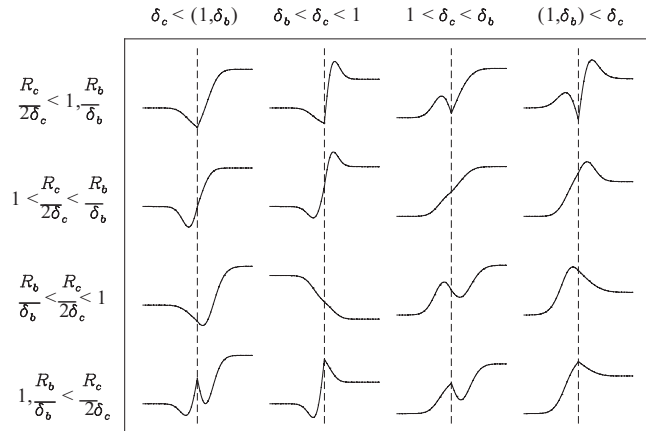


FIG. 5. Sketch of the 16 types of base-state density profiles for a stationary reaction front,  $\alpha = 0$ . The vertical dashed lines correspond to the position of the stationary reaction front.

$$U_1 < R_c < R_b L_2 \quad \text{for } \alpha > 0,$$

$$U_2 < R_c < R_b L_1 \quad \text{for } \alpha < 0.$$

A sufficient condition for a monotonically increasing density profile to exist for all values of  $\alpha$  is when

$$R_b > \delta_b > \delta_c > 1$$

for  $R_c$  within an appropriate range, but this is not a necessary condition.

We recall that this problem contains six dimensionless parameters, namely,  $\mathcal{D}$ ,  $R_b$ ,  $R_c$ ,  $\varphi$ ,  $\delta_b$ , and  $\delta_c$ . However, now that the various density profiles and differential diffusion instabilities have been classified within this parameter space, it should now be much easier to identify suitable parameters to yield a variety of different types of instabilities.

#### IV. CONCLUSIONS

Buoyancy-driven instabilities around  $A + B \rightarrow C$  reaction fronts exhibit a much richer possibility of dynamics than the nonreactive case. This is mainly due to the fact that the two-species problem of the nonreactive stratification of  $A$  on top of  $B$  is replaced by a three-species problem ( $A, B, C$ ) where the product  $C$  is generated *in situ* as soon as  $A$  and  $B$  are put in contact in the reactive case. The parameter space of the reactive case encompasses six parameters which affect the density profile, namely, the initial ratio  $\varphi$  of concentrations of  $A$  and  $B$ , the ratios of diffusion coefficients  $\delta_{b,c}$  and of solutal expansion coefficients  $R_{b,c}$ , as well as the Damköhler number  $\mathcal{D}$ . Here we have classified the various possible instability

scenarios in this parameter space, showing that the reactive case can feature 62 different types of density profiles, where the nonreactive one can only have six different cases. Our classification opens the way to a better understanding of the instability mechanisms at play for a given set of parameters and calls for further experimental and theoretical analysis of the nonlinear dynamics to be observed in each case.

#### ACKNOWLEDGMENT

A.D. acknowledges Prodex as well as the FRS-FNRS under the PDR-FORECAST project for financial support.

- 
- [1] J. A. Pojman and I. R. Epstein, *An Introduction to Nonlinear Chemical Dynamics Oscillations, Waves, Patterns, and Chaos* (Oxford University Press, New York, 1998).
  - [2] A. De Wit, K. Eckert, and S. Kalliadasis, *Chaos* **22**, 037101 (2012).
  - [3] A. Zalts, C. El Hasi, D. Rubio, A. Urena, and A. D'Onofrio, *Phys. Rev. E* **77**, 015304 (2008).
  - [4] K.-I. Tanoue, H. Ikemoto, M. Yoshitomi, and T. Nishimura, *Thermal Sci. Eng.* **17**, 121 (2009).
  - [5] K.-I. Tanoue, M. Yoshitomi, and T. Nishimura, *J. Chem. Eng. Jpn.* **42**, 255 (2009).
  - [6] B. A. Grzybowski, *Angew. Chem. Int. Ed.* **50**, 40 (2011).
  - [7] K. Tsuji and S. C. Müller, *J. Phys. Chem. Lett.* **3**, 977 (2012).
  - [8] C. Almarcha, P. M. J. Trevelyan, P. Grosfils, and A. De Wit, *Phys. Rev. Lett.* **104**, 044501 (2010).
  - [9] C. Almarcha, P. M. J. Trevelyan, L. Riolfo, A. Zalts, C. El Hasi, A. D'Onofrio, and A. De Wit, *J. Phys. Chem. Lett.* **1**, 752 (2010).
  - [10] S. Kuster, L. A. Riolfo, A. Zalts, C. El Hasi, C. Almarcha, P. M. J. Trevelyan, A. De Wit, and A. D'Onofrio, *Phys. Chem. Chem. Phys.* **13**, 17295 (2011).
  - [11] C. Almarcha, Y. R'Honi, Y. De Decker, P. M. J. Trevelyan, K. Eckert, and A. De Wit, *J. Phys. Chem. B* **115**, 9739 (2011).
  - [12] L. Lemaigre, M. A. Budroni, P. Grosfils, and A. De Wit, *Phys. Fluids* **25**, 014103 (2013).
  - [13] L. Rongy, P. M. J. Trevelyan, and A. De Wit, *Phys. Rev. Lett.* **101**, 084503 (2008).
  - [14] L. Rongy, P. M. J. Trevelyan, and A. De Wit, *Chem. Eng. Sci.* **65**, 2382 (2010).
  - [15] S. H. Hejazi and J. Azaiez, *J. Fluid Mech.* **695**, 439 (2012).
  - [16] S. H. Hejazi and J. Azaiez, *Water Resour. Res.* **49**, 4607 (2013).
  - [17] H. Alhumade and J. Azaiez, *Chem. Eng. Sci.* **101**, 46 (2013).
  - [18] M. C. Kim, *Chem. Eng. Sci.* **112**, 56 (2014).
  - [19] J. Fernandez, P. Kurowski, P. Petitjeans, and E. Meiburg, *J. Fluid Mech.* **451**, 239 (2002).
  - [20] P. M. J. Trevelyan, C. Almarcha, and A. De Wit, *J. Fluid Mech.* **670**, 38 (2011).
  - [21] J. S. Turner, *Buoyancy Effects in Fluids* (Cambridge University Press, Cambridge, 1979).
  - [22] C. A. Cooper, R. J. Glass, and S. W. Tyler, *Water Resour. Res.* **33**, 517 (1997).
  - [23] S. E. Pringle and R. J. Glass, *J. Fluid Mech.* **462**, 161 (2002).
  - [24] J. Carballido-Landeira, P. M. J. Trevelyan, C. Almarcha, and A. De Wit, *Phys. Fluids* **25**, 024107 (2013).
  - [25] J. Crank, *The Mathematics of Diffusion*, 2nd ed. (Oxford University Press, New York, 1975).
  - [26] D. A. Nield and A. Bejan, *Convection in Porous Media* (Springer, New York, 2006).
  - [27] L. Gálfi and Z. Rácz, *Phys. Rev. A* **38**, 3151 (1988).
  - [28] Z. Koza, *J. Stat. Phys.* **85**, 179 (1996).
  - [29] M. Sinder and J. Pelleg, *Phys. Rev. E* **62**, 3340 (2000).
  - [30] J. Gandhi and P. M. J. Trevelyan, *J. Eng. Math.* **86**, 31 (2014).